

The Hydrodynamic Origin of Neutron Star Kicks

J. Nordhaus^{1,2,3,4*}, T. D. Brandt⁴, A. Burrows⁴, A. Almgren⁵

¹ *Center for Computational Relativity and Gravitation, Rochester Institute of Technology, Rochester, NY 14623, U.S.A.*

² *National Technical Institute for the Deaf, Rochester Institute of Technology, Rochester, NY 14623, U.S.A.*

³ *Department of Physics and Astronomy, University of Rochester, Rochester, NY 14627, U. S. A.*

⁴ *Department of Astrophysical Sciences, Princeton University, Princeton, NJ 08544, U.S.A.*

⁵ *Computational Research Division, Lawrence Berkeley National Lab, Berkeley, CA 94720, U.S.A.*

Submitted XXX

ABSTRACT

We present results from a suite of axisymmetric, core-collapse supernova simulations in which hydrodynamic recoil from an asymmetric explosion produces large proto-neutron star (PNS) velocities. We use the adaptive-mesh refinement code CASTRO to self-consistently follow core-collapse, the formation of the PNS and its subsequent acceleration. We obtain recoil velocities of up to 620 km s^{-1} at $\sim 1 \text{ s}$ after bounce. These velocities are consistent with the observed distribution of pulsar kicks and with PNS velocities obtained in other theoretical calculations. Our PNSs are still accelerating at several hundred km s^{-1} at the end of our calculations, suggesting that even the highest velocity pulsars may be explained by hydrodynamic recoil in generic, core-collapse supernovae.

Key words: supernovae: general – hydrodynamics – stars: interiors – pulsars – neutron stars

1 INTRODUCTION

At birth, pulsars achieve velocities well above those of their progenitor population (Gunn and Ostriker 1970; Lyne and Lorimer 1994). These pulsar “kicks” typically range from 200 km s^{-1} to 400 km s^{-1} , with the fastest neutron stars achieving velocities near, or in excess of, 1000 km s^{-1} (Lyne and Lorimer 1994; Chatterjee et al. 2005; Hobbs et al. 2005). The current distribution of observed pulsar velocities is Maxwellian, hinting at a common acceleration mechanism (Hansen and Phinney 1997; Hobbs et al. 2005; Zou et al. 2005; Faucher-Giguère and Kaspi 2006).

Many scenarios have been proposed for the origin of pulsar recoil and neutron star kicks. Popular mechanisms often require strongly magnetized systems, exotic neutrino physics, and/or rapid rotation to produce substantial kicks. For example, in the presence of strong magnetic fields, neutrino-matter interactions can generate neutron star velocities on the order of a few hundred km s^{-1} by producing $\sim 1\%$ dipole asymmetries (Lai and Qian 1998; Nardi and Zuluaga 2001; Lai et al. 2001; Kusenko and Segrè 1999; Lambiase 2005; Barkovich et al. 2004; Fuller et al. 2003; Kishimoto 2011). Many of these scenarios require magnetic fields in the magnetar range (i.e. 10^{14-16} G) and may not produce substantial kicks in typical core-collapse supernovae. Other sce-

narios involve jet/counter-jet misalignment launched near the proto-neutron star (PNS). In such situations, the jets accompany an associated gamma-ray burst (GRB) or form through magneto-rotational processes during core collapse (Cen 1998; Khokhlov et al. 1999; Sawai et al. 2008; Papish and Soker 2011). These scenarios require rapid rotation and therefore, may only manifest in a small subset of core-collapse events.

If neutron star kicks are a generic outcome of core collapse, then a natural explanation is recoil during an asymmetric supernova explosion. In the current, most sophisticated simulations, the bounce shock, launched when the equation of state stiffens at nuclear densities, stalls due to thermal energy losses from neutrino emission and dissociation of nuclei into nucleons. The stalled shock itself is subject to hydrodynamic and neutrino-driven instabilities, which manifest as prominent low-order ℓ -mode oscillations in axisymmetric simulations of non-rotating progenitors (Blondin et al. 2003; Scheck et al. 2004; Buras et al. 2006; Scheck et al. 2006; Burrows et al. 2007a; Blondin and Mezzacappa 2007; Ott et al. 2008; Fernández and Thompson 2009; Nordhaus et al. 2010b,a; Fernández 2010; Brandt et al. 2011). At the onset of shock revival, the PNS may recoil if large-scale asymmetries are present during the ensuing supernova explosion. While the mechanism by which core-collapse supernova progenitors explode is not fully understood, the most probable scenario involves absorption of neutrinos in the post-shock “gain region” (Bethe and Wilson 1985) and likely

* NSF Astronomy and Astrophysics Postdoctoral Fellow; E-mail: nordhaus@astro.rit.edu

requires the development of multi-dimensional instabilities in fully three-dimensional radiation-hydrodynamic simulations to succeed (Nordhaus et al. 2010b). Nonetheless, recoil from an asymmetric neutrino-driven explosion presents a natural mechanism by which PNSs achieve high velocities (Burrows and Hayes 1996; Scheck et al. 2004, 2006; Nordhaus et al. 2010a; Wongwathanarat et al. 2010) and appears to be supported by recent X-ray observations of the Cassiopeia A supernova remnant (Hwang and Laming 2011).

Computational studies of recoil require multi-dimensional, radiation-hydrodynamics calculations which start at the onset of collapse and follow the dynamics self-consistently. This includes the formation of the PNS, the explosion, the propagation of the shock front through the stellar envelope and eventually, decoupling of the PNS from the surrounding material. Such an approach is computationally challenging and as such, various techniques have been adopted to make the computations tractable. One popular approach is to commence the calculations after bounce by mapping spherically symmetric solutions onto a multi-dimensional grid and excising the PNS from the computational domain (Scheck et al. 2004, 2006; Wongwathanarat et al. 2010). This requires one to infer a PNS kick through a rigid, impenetrable inner boundary, but allows one to track the supernova explosion for several seconds and to distances greater than 10,000 km. While this approach is appealing, it must be checked by simulations which include the PNS in the computational domain.

Recently, we have carried out the first axisymmetric, radiation-hydrodynamic simulation of recoil with the multi-group, arbitrary, Lagrangian-Eulerian code VULCAN/2D (Nordhaus et al. 2010a). By transitioning from a spherical-polar mesh to a pseudo-Cartesian mesh at the center of the domain, we self-consistently tracked the PNS's formation and off-center motion. This calculation was computationally expensive, as it employed multi-group flux limited diffusion neutrino transport and followed the supernova explosion until the shock reached the 5,000 km radial outer boundary of the domain. At that time, the PNS had reached a velocity of $\sim 150 \text{ km s}^{-1}$ but had yet to fully decouple from the ejecta. The PNS recoil was due almost entirely to hydrodynamical processes and was consistent with previous excised-core calculations (Scheck et al. 2004, 2006). Asymmetric neutrino emission contributed $\sim 2\%$ to the overall kick magnitude. This suggests that neutrinos play no significant role in accelerating neutron stars to high velocities during typical core-collapse supernovae. At the end of the calculation, significant acceleration ($\sim 350 \text{ km s}^{-2}$), in addition to the degree of asymmetry in the ejecta, suggested that higher PNS velocities were possible. Verifying these estimates requires tracking the supernova shock to greater radial distances and later times.

To expand upon the work of Nordhaus et al. (2010a), we carry out a suite of axisymmetric collapse calculations with the adaptive-mesh-refinement (AMR), radiation-hydrodynamics code, CASTRO (Almgren et al. 2010; Zhang et al. 2011). By employing AMR and a simplified form of transport (see Sec. 2), we expand the domain to a radial distance of 10,000 km and perform multiple calculations. Our PNSs achieve recoil velocities ranging from tens of km s^{-1} up to $\sim 620 \text{ km s}^{-1}$. In general, the magnitude of the recoil depends on the degree of asymmetry at the time of explosion

and the energy of the explosion itself (Burrows et al. 2007b). In Sec. 3, we discuss the physical processes that accelerate the PNS. In Sec. 4, we compare our results with previous work before concluding and discussing future work in Sec. 5.

2 COMPUTATIONAL METHODOLOGY

We carry out our simulations using the AMR, radiation-hydrodynamics code, CASTRO (Almgren et al. 2010; Zhang et al. 2011). CASTRO is a finite-volume, Eulerian code which employs an unsplit version of the piecewise parabolic method (PPM) for the hydrodynamics and a multigrid Poisson solver to handle self-gravity. To facilitate multiple calculations, we simplify our radiation transport by using radius- and temperature-dependent prescriptions for the neutrino heating and cooling rates \mathcal{H} and \mathcal{C} . We solve the fully compressible equations of hydrodynamics:

$$\begin{aligned} \partial_t \rho &= -\nabla \cdot (\rho \mathbf{v}) \\ \partial_t (\rho \mathbf{v}) &= -\nabla \cdot (\rho \mathbf{v} \mathbf{v}) - \nabla p + \rho \mathbf{g} \\ \partial_t (\rho E) &= -\nabla \cdot (\rho \mathbf{v} E + p \mathbf{v}) + \rho \mathbf{v} \cdot \mathbf{g} + \rho (\mathcal{H} - \mathcal{C}), \end{aligned} \quad (1)$$

where p , T , ρ , \mathbf{g} , and \mathbf{v} are the fluid pressure, temperature, density, gravitational acceleration, and velocity. The specific total energy is given as $E = e + \frac{1}{2}v^2$, where e represents the internal energy. Neutrino heating and cooling occur via the super-allowed charged-current reactions involving free nucleons, electrons, protons, electron neutrinos and anti-electron neutrinos. We use the heating and cooling rates derived in Janka (2001) and previously used by Murphy and Burrows (2008) and Nordhaus et al. (2010b). These rates, assuming the electron and anti-electron neutrino luminosities, L_{ν_e} and $L_{\bar{\nu}_e}$, to be equal, are

$$\mathcal{H} = 1.544 \times 10^{20} \left(\frac{L_{\nu_e}}{10^{52} \text{ erg s}^{-1}} \right) \left(\frac{T_{\nu_e}}{4 \text{ MeV}} \right)^2 \times \left(\frac{100 \text{ km}}{r} \right)^2 (Y_n + Y_p) e^{-\tau_{\text{eff}}} \left[\frac{\text{erg}}{\text{g s}} \right] \quad (2)$$

and

$$\mathcal{C} = 1.399 \times 10^{20} \left(\frac{T}{2 \text{ MeV}} \right)^6 (Y_n + Y_p) e^{-\tau_{\text{eff}}} \left[\frac{\text{erg}}{\text{g s}} \right], \quad (3)$$

where T_{ν_e} is the electron neutrino temperature, r is the distance from the center of the star, Y_n and Y_p are the neutron and proton fractions, and τ_{eff} is an effective optical depth for electron and anti-electron neutrinos (see Eqs. 6 & 7 of Hanke et al. (2011)). The factor $e^{-\tau_{\text{eff}}}$ effects a transition between the dense inner regions, where neutrinos are trapped and heating and cooling are suppressed, to the outer, optically thin regions. To avoid the prohibitive cost of global calculations, we fit τ_{eff} as a function of density by post-processing models and applying Eq. 6 of Hanke et al. (2011). In the transition region, $10^{-2} \lesssim \tau_{\text{eff}} \lesssim 1$, the resulting power-law fits give root-mean-square residuals of $\sim 10\%$ in $e^{-\tau_{\text{eff}}}$. Note also that the bulk of neutrino heating occurs within the inner few hundred kilometers and falls off rapidly with radial distance. The electron fraction, Y_e , evolves on infall via a density prescription given in Liebendörfer et al. (2005) and previously employed by Murphy and Burrows (2008) and

Nordhaus et al. (2010b). To close the equations, we use the sophisticated, finite temperature, nuclear equation of state of Shen et al. (1998).

The current theoretical consensus holds that most 2D core-collapse simulations do not produce neutrino-induced explosions for the majority of progenitors without supplementing the neutrino luminosity (Burrows et al. 2007b; Ott et al. 2008; Nordhaus et al. 2010a; Brandt et al. 2011; Fujimoto et al. 2011). However, explosions in axisymmetric simulations have been obtained after ~ 600 ms for a $15 M_{\odot}$ progenitor when a soft nuclear equation of state and variable Eddington factor closure technique are employed (Marek and Janka 2009). We therefore induce explosions by varying the neutrino driving luminosity L_{ν_e} ($= L_{\bar{\nu}_e}$) from 2.1 to 2.5×10^{52} erg s $^{-1}$. These values are comparable to the time-dependent values achieved in 2D calculations with detailed neutrino transport (Ott et al. 2008; Brandt et al. 2011). Our simplified transport scheme couples this energy somewhat more efficiently to the post-shock region, and our results should be checked by future studies that employ sophisticated, but computationally expensive, neutrino transport. We hold the driving luminosity L_{ν_e} fixed in each calculation, but vary it from run to run. Our simplified transport method, in conjunction with AMR, allows us to follow collapse, formation of the PNS, and any subsequent acceleration due to the supernova explosion.

We use the $15 M_{\odot}$, red-supergiant, non-rotating, solar-metallicity progenitor of Woosley and Weaver (1995). Our simulations begin at the onset of core-collapse, continue through the formation of the PNS and the launching, stalling, and revival of the bounce shock, and end when the shock approaches the edge of the computational domain. We employ a 2D, 10,000-km by 20,000-km domain discretized with a uniform coarse grid of 64 by 128 cells covering the full 180° range in polar angle. Within 200 km of the PNS, we use 4 AMR levels, each increasing the resolution by a factor of 4, giving a minimum cell size of ~ 0.3 km. Exterior to 200 km, the adaptive mesh tracks the high entropy, shocked material.

We index our eight simulations by their driving electron neutrino luminosity L_{ν_e} in units of 10^{52} erg s $^{-1}$, from $L_{2.1}$ to $L_{2.5}$. For each simulation, we follow the explosion for ~ 1 second of post-bounce evolution. For all but the $L_{2.1}$ model, the calculation ends when the shock approaches the edge of the computational domain, 10,000 km from the PNS. At this point the total momentum on the grid is conserved to within $\sim 1\%$ of the core's final value.

3 ACCELERATION OF THE PNS

The hydrodynamic flow behind the stalled shock is turbulent, and is soon deformed by the development of low-mode hydrodynamic and neutrino-driven instabilities (Burrows et al. 1995; Blondin et al. 2003; Scheck et al. 2004, 2006; Blondin and Mezzacappa 2007; Fernández 2010). This guarantees an asymmetric distribution of material when neutrino heating revives the stalled shock. The ensuing asymmetric explosion accelerates the PNS as the shock propagates through the stellar envelope.

To understand the physical processes governing the recoil, we first present the PNS velocities obtained in our sim-

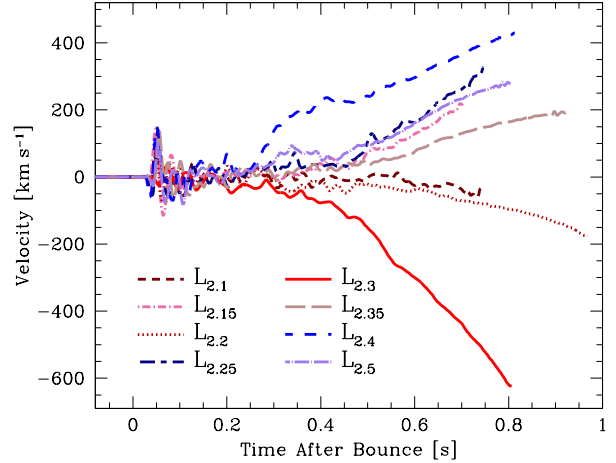


Figure 1. PNS recoil velocities as a function of time after formation of the bounce shock. The subscript in the simulation names refers to the electron neutrino, ν_e , and anti-electron neutrino, $\bar{\nu}_e$, luminosities, each in units of 10^{52} erg s $^{-1}$ (see Eqs. (2) and (3) and Table 1).

ulations. We compute the core positions as the centroids of the density distributions and differentiate to obtain the velocities, which we show as functions of time in Figure 1. The subscript in each simulation label indicates the driving L_{ν_e} in units of 10^{52} erg s $^{-1}$. The value of the driving $L_{\bar{\nu}_e}$ is taken to be the same, thus yielding a total driving luminosity in each simulation of $L_{\text{tot}} = L_{\nu_e} + L_{\bar{\nu}_e} = 2L_{\nu_e}$. We obtain PNS velocities ranging from tens to many hundreds of km s $^{-1}$. The highest velocity PNS (solid red curve in Fig. 1) reaches a speed of 624 km s $^{-1}$ after ~ 800 ms of post-bounce evolution, and is still accelerating at ~ 1000 km s $^{-2}$.

Figure 2 depicts the evolution of a representative run (model $L_{2.4}$). The left column presents the evolution of electron fraction, Y_e , over the inner ~ 200 km, as the explosion progresses. The middle of the computational domain is marked by a black line ($Z = 0$). The PNS is clearly visible as the deleptonized blue region, which begins at $Z = 0$ and moves off-center. The right column shows the global evolution of the anisotropic supernova shock, with the color map depicting entropy. The explosion occurs primarily in the $-Z$ direction while the PNS recoils in the $+Z$ direction. By ~ 800 ms after bounce, the PNS has largely decoupled from its surroundings. The middle column shows the density distribution with the shock outlined in pink. A high-density region above the PNS combines with a low-density region below it to gravitationally accelerate the PNS in the $+Z$ direction.

3.1 Physics of the Recoil

To determine the physical processes governing the movement of the PNS, we post-process our results by computing the hydrodynamic acceleration \vec{a}_c of the core due to anisotropic pressure forces, momentum flux, and gravitational forces. The Eulerian equations of hydrodynamics give

$$\vec{a}_c = \dot{\vec{v}}_c \approx \int_{r>r_c} \frac{G\vec{r}}{r^3} dm - \frac{1}{M_c} \left[\oint_{r=r_c} P d\vec{S} + \oint_{r=r_c} \rho \vec{v} dS \right], \quad (4)$$

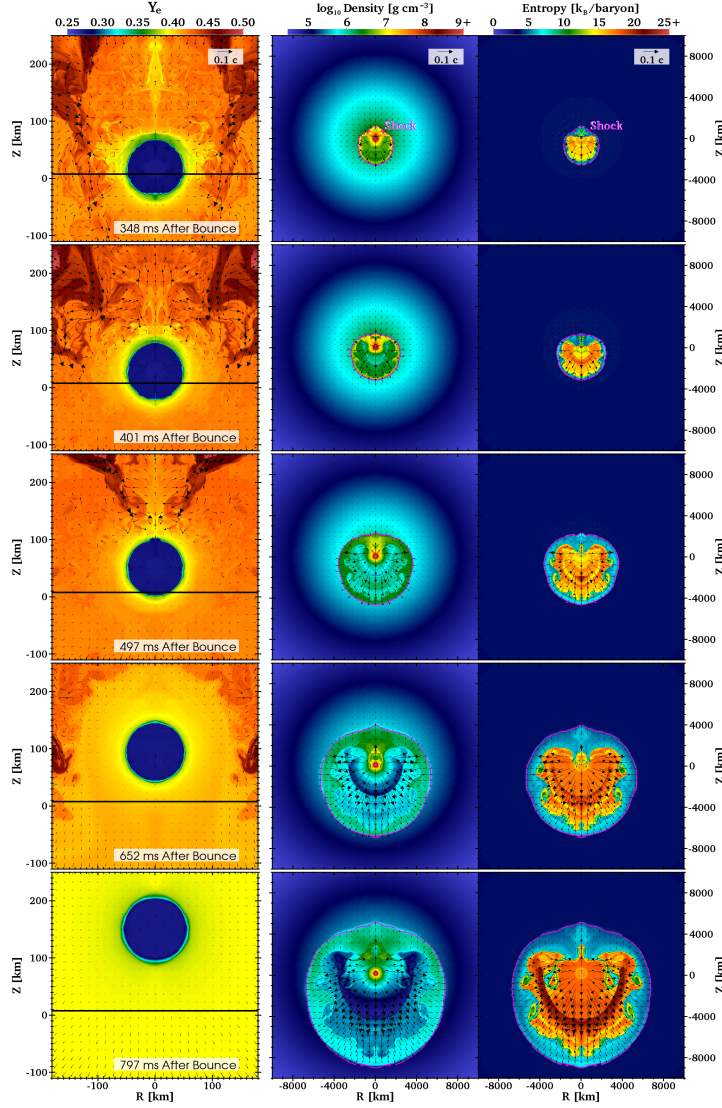


Figure 2. The left column shows the evolution of the inner ~ 200 km of the simulation domain for model L_{2.4}. The color map depicts the electron fraction, Y_e , with velocity vectors overlaid; the black lines indicate $Z = 0$. The color map for the middle column depicts density. The pink curve shows the location of the shock. Exterior to the shock, the flow is radially inward. The right column panels show the entropy evolution of the explosion. The steep entropy jump just interior to the shock depicts the region where nucleons are reassociated into nuclei and alpha particles. At 707 ms after bounce, the PNS wind is seen as the dark blue region interior to the shock in the middle panel. The supernova explosion primarily occurs in the $-Z$ direction, while the PNS recoils in the $+Z$ direction. At ~ 800 ms after bounce, the PNS has largely decoupled from the surrounding material, but is still being accelerated by the gravitational pull of slow-moving ejecta in the $+Z$ direction (see Fig. 3).

where ρ is the density, M_c and \vec{v}_c are the mass and mean velocity of the core, P is the gas pressure, \vec{v} is the fluid velocity, v_r is the radial component of the velocity, and r_c is a fiducial spherical radius (Scheck et al. 2006; Nordhaus et al. 2010a).

The three terms in Eq. (4) represent the contributions to the acceleration from the gravitational field of matter exterior to r_c , anisotropic gas pressure, and momentum flux through r_c , respectively. The first term assumes a spherically-symmetric matter distribution interior to r_c , which in practice is an excellent approximation. In the limit of an isotropic explosion, no acceleration occurs and each term vanishes individually.

Equation (4) includes contributions from hydrodynamic processes, but neglects radiation pressure asymmetries, which are not captured by our heating and cooling prescription (Eqs. (2)-(3)). In our previous calculations, which performed radiative transfer using multi-group flux-limited diffusion, neutrino momentum contributed $\lesssim 2\%$ of the overall kick (Nordhaus et al. 2010a). This is consistent with previous studies that found neutrino radiation pressure to contribute $\sim 5\%$ to the final kick velocity (Scheck et al. 2004, 2006).

The relative contributions of the terms in Eq. (4) depend on the properties of the flow and the explosion dynamics. As a consequence of the explosion, the PNS generically recoils away from the high-velocity ejecta and towards the lower-velocity ejecta. However, the interpretation of the kick is not as straightforward as Eq. (4) would suggest. As discussed in Section III of Nordhaus et al. (2010a), pressure and gravity do work on fluid elements; anisotropic pressure or gravitational forces at a small value of r_c will appear as anisotropic momentum flux at a larger value of r_c .

Using a fiducial radius of $r_c = 200$ km and integrating Eq. 4 from core bounce, Figure 3 shows the decomposition of the PNS kick into three components for models $L_{2.25}$ (top panel), $L_{2.3}$ (middle panel) and $L_{2.4}$ (bottom panel). Note that the velocities have been reflected for model $L_{2.3}$. In each panel, the dash-dotted black curve represents the smoothed centroid velocity, while the solid red curve is the sum of the three terms in Eq. (4). The gravitational component (short-dashed green curve) dominates the late-time evolution in all three simulations. The anisotropic pressure term (dot-dashed pink curve) flattens towards the end of each run as the PNS decouples from the ejecta.

Model $L_{2.3}$ achieved the highest kick velocity in our suite of simulations, more than 620 km s^{-1} at ~ 800 ms after bounce. The middle panel of Figure 3 shows its velocity evolution, decomposed using Eq. (4) and inverted to facilitate comparison with models $L_{2.25}$ and $L_{2.4}$. Anisotropic pressure and momentum flux (dot-dashed pink and long-dashed blue lines, respectively) contributed almost nothing to the kick after ~ 400 ms from core bounce. Driven by the gravitational term in Eq. (4), this model was still accelerating at more than 1000 km s^{-2} when the shock reached the edge of the computational domain.

While they did not achieve as large a PNS velocity as $L_{2.3}$, models $L_{2.25}$ and $L_{2.4}$ were still accelerating at ~ 1000 and $\sim 600 \text{ km s}^{-2}$, respectively, at the end of our calculations. In both cases, and particularly for the $L_{2.4}$ model, this acceleration was dominated by the gravitational term in Eq. (4). Figure 2 clearly shows the PNS and ejecta in model $L_{2.4}$ decoupling at ~ 650 ms after bounce (second panel from bottom), and having almost completely decoupled by ~ 800 ms after bounce.

The three models presented here comprise a representative sample of our simulation results. Table 1 presents additional information on each of our runs, including the velocity, the explosion energy E_{exp} , and α , a dimensionless measure of the degree of asymmetry, at the end of the calculations. The parameters α and E_{exp} are defined by Eqs. (5) and (6) in the following section. All of our calculations, except for $L_{2.1}$, ended when the shock approached a radius of 10,000 km; model $L_{2.1}$ ended with $R_{\text{shock}} = 3300$ km. For a detailed discussion of the limitations of our approach, the effect of fixing the neutrino luminosities and the reliability of

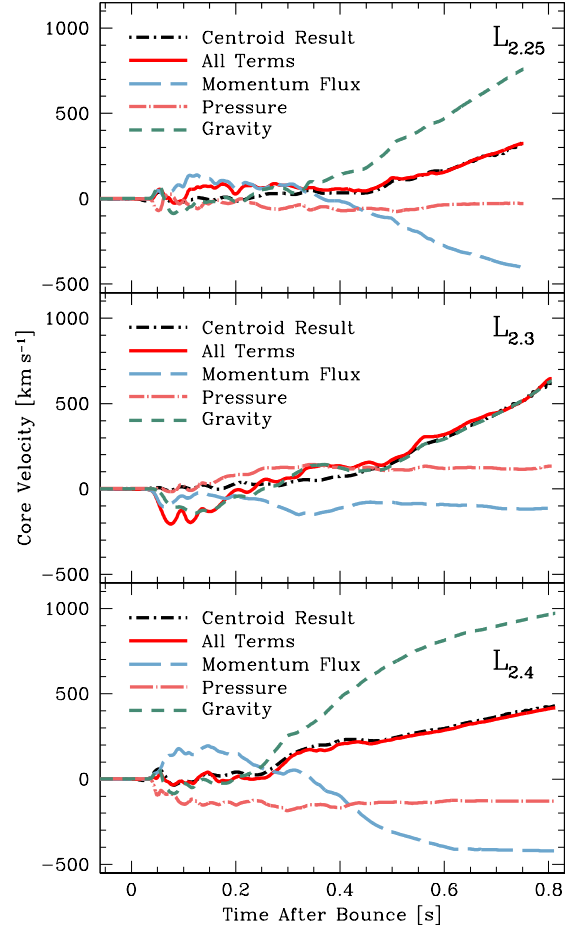


Figure 3. Decomposed PNS kick velocities for models $L_{2.25}$ (top panel), $L_{2.3}$ (middle panel) and $L_{2.4}$, obtained by integrating Eq. (4) from bounce. We have inverted the velocities for the $L_{2.3}$ run. The dash-dotted-black curve depicts the PNS velocity computed using the centroid of the density, while the solid red curve shows the contributions to the kick from momentum flux (long-dashed blue curve), gravity (dashed green curve) and pressure (dash-dot pink curve). In each run, the PNS is still accelerating at more than 500 km s^{-2} at the end of the calculation, and this acceleration is dominated by the gravitational term.

the late-time acceleration and explosion energies see Section 3.3.

3.2 Asymmetries in the Ejecta and Explosion Energies

The acceleration of the PNS depends on the dynamics of the explosion and the evolution of the asymmetry of the shocked material. This asymmetry may be quantified in various ways (Scheck et al. 2006; Burrows et al. 2007b); here, we adopt

$$\alpha \equiv \langle v_z \rangle / \langle |v| \rangle, \quad (5)$$

where $\langle \rangle$ denotes a mass-weighted average over the post-shock region with $r > 100$ km (thereby excluding the PNS itself). This choice is similar to the α presented in Scheck et al. (2006).

Figure 4 shows the evolution of α for models $L_{2.4}$ (solid blue curve) and $L_{2.5}$ (dashed blue curve). The solid red and

Table 1. Parameters at the end of the simulation, when $R_{\text{shock}} \sim 10,000$ km; α and E_{exp} are calculated using Eqs. (5) and (6), respectively. Model L_{2.1} ended with $R_{\text{shock}} = 3300$ km. Note that the PNS wind contributes $\sim 50\%$ of the explosion energies listed below.

Model	v_{PNS} [km s ⁻¹]	E_{exp} [10 ⁵¹ erg]	α
L _{2.1}	-40	0.29	0.026
L _{2.15}	212	0.69	-0.25
L _{2.2}	-186	0.89	0.08
L _{2.25}	315	0.69	-0.23
L _{2.3}	-624	1.13	0.23
L _{2.35}	194	1.28	-0.06
L _{2.4}	431	1.23	-0.15
L _{2.5}	276	0.99	-0.10

dashed red curves depict the PNS recoil velocities for the L_{2.4} and L_{2.5} models respectively. Our suite of simulations produced final values of α between -0.25 and 0.25 (see Table 1). Since momentum is conserved, larger values of α lead to larger PNS recoil velocities.

Figure 6 shows the position of the shock at the end of the calculation for five of our models; models with a negative kick have been reflected. While the shock asymmetry does correlate with the kick velocity, the magnitude of the kick depends on the distribution of matter behind the shock, which we parametrize using α .

The third column of Table 1 shows the explosion energy at the end of the simulation, defined as the total energy of all unbound material on the grid,

$$\int_{E_{\text{tot}} > 0} \rho \left(u_{\text{int}} + \frac{v^2}{2} - \frac{G}{r^2} M_{\text{enc}} \right) d^3 \mathbf{x}, \quad (6)$$

where u_{int} is the specific internal energy and M_{enc} is the mass interior to the fluid element. At the end of our calculations, the internal energy of shocked material dominates the kinetic energy by a factor of ~ 3 – 5 , and the explosion energy is still increasing due to sustained neutrino heating (Eq. (2)). The bulk of this heating occurs primarily within the first few hundred kilometers of the PNS and is driving the late-time PNS wind.

The internal energy of shocked material will ultimately be converted into kinetic energy by $p dV$ work. In this limit, the PNS kick will be a function of the anisotropy of the ejecta and E_{exp} . While the explosion will be nearly spherical in the outer envelope, the anisotropy in the inner mass shells should freeze out at values close to those indicated in Table 1. This anisotropy in the inner ejecta velocities, with the bulk of the ejecta traveling opposite to the recoiling PNS, should be observable in the supernova remnant and is a specific prediction of our model.

Figure 5 shows the total explosion energy (solid blue curve) as a function of time for model L_{2.4}. The explosion energy of material in the bottom half of the computational grid ($Z < 0$) is depicted by the dot-dashed green curve, while the explosion energy of material in the top half of the computational grid ($Z > 0$) is depicted by the dashed red curve. Consistent with Fig. 2, this demonstrates that model L_{2.4} explodes primarily in the $-Z$ direction. The bottom panel of Fig. 5 shows the PNS mass as a function of time (solid blue curve) and the total mass of shocked, bound material exterior to the core (dot-dashed red curve). By the

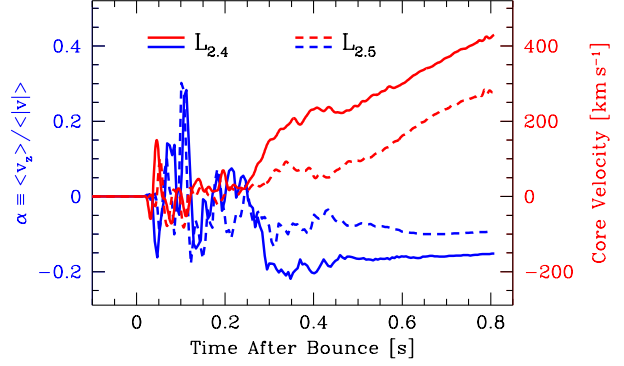


Figure 4. The blue curves show the evolution of α (Eq. (5)) for models L_{2.4} (solid) and L_{2.5} (dashed), while the red curves show the core recoil velocity as a function of time. The core velocity is always opposite the ejecta asymmetry due to conservation of momentum.

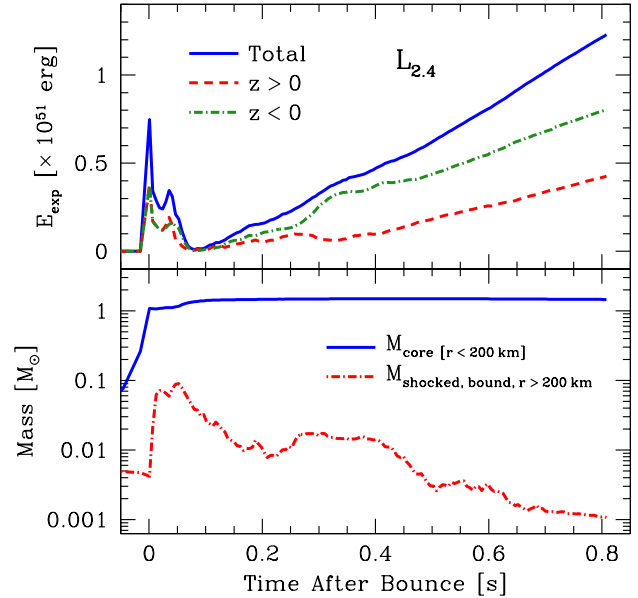


Figure 5. The top panel shows the explosion energy (Eq. (6)) as a function of time for model L_{2.4}. The solid blue curve depicts the total explosion energy. The explosion energy of material with $Z < 0$ is shown by the dot-dashed green curve while the explosion energy of material with $Z > 0$ is shown by the dashed red curve. The bottom panel presents the PNS mass (solid blue curve) as a function of time; its final value is $1.45 M_{\odot}$. The dot-dashed red curve in the bottom panel shows the total shocked, bound mass exterior to the core as a function of time. At the end of the simulation, only $\sim 10^{-3} M_{\odot}$ of shocked material outside the PNS remains bound.

end of model L_{2.4}, the PNS mass is $1.45 M_{\odot}$ while there is little shocked, bound matter outside the PNS itself.

3.3 Late-Time Evolution

Our simplified transport scheme allows us to perform multiple calculations of the inner regions of a core-collapse su-

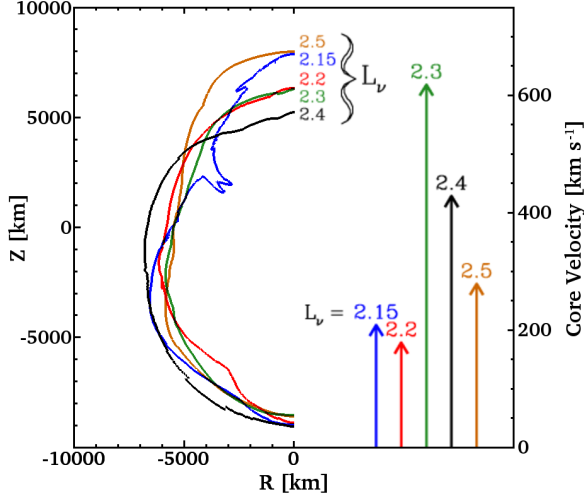


Figure 6. The position of the outer edge of the gain region toward the end of the calculations. Runs with negative PNS velocity have been reflected in this plot. The arrows depict the core velocity for each run (right axis).

pernova. To date, only one time-dependent, multi-group, flux-limited diffusion, neutrino transport kick calculation, which includes the PNS on the computational grid, exists in the literature (Nordhaus et al. 2010a). As computational methods and resources improve, it will become possible to self-consistently connect the PNS kick with the large-scale properties of the ejecta. In this section, we discuss the late-time evolution of our simulations and some of the limitations of our approach.

As previously mentioned, the magnitude of the PNS kick will increase with the degree of asymmetry in the ejecta and the explosion energy of the supernova. At the end of our calculations, the shocked matter’s internal energy exceeds its kinetic energy by a factor of ~ 3 – 5 . Adiabatic expansion will convert this internal energy into kinetic energy as the shock propagates through the stellar envelope.

Our constant driving L_{ν_e} also deposits energy into the expanding ejecta, both by neutrino absorption in the gain region and by driving a $\sim 0.1 M_{\odot} s^{-1}$ wind from the surface of the PNS. This late-time wind contributes $\sim 50\%$ of the explosion energy at the end of each simulation and typically contains $\sim 0.05 M_{\odot}$ of material. While neutrino-driven winds from the PNS are expected (Burrows et al. 1995), future improvements to this work should include more sophisticated transport approaches which naturally incorporate time-variable neutrino luminosities.

We tested the effect of decaying neutrino driving luminosities by restarting model $L_{2.3}$ 400 ms after bounce with an exponentially decreasing driving luminosity. We used an exponential decay timescale of 1 second, giving a $\sim 35\%$ reduction in L_{ν_e} at the end of our calculation. As a result of the lower energy injection rate, the late-time PNS wind decreased by nearly a factor of two, the PNS took longer to decouple from the post-shock material, and the final PNS velocity was $\sim 25\%$ lower. Still, the PNS was accelerating gravitationally at $\sim 1000 \text{ km s}^{-1}$, nearly as fast as in the model with a constant driving luminosity.

We also note that our calculations end when the shock reaches a fixed radius of $\sim 10,000$ km, rather than after a fixed amount of post-bounce time. The total amount of energy injected into our models thus varies widely, making it difficult to connect the derived explosion energies with our observed kick velocities.

4 COMPARISON WITH PREVIOUS NUMERICAL WORK

Previous computational studies of pulsar recoil have employed various simplifications and approximations to make the calculations tractable. These approaches include excising the PNS from the computational domain, starting the calculations ~ 20 ms after bounce, and employing simplified neutrino transport schemes (Scheck et al. 2004, 2006; Wongwathanarat et al. 2010). The exclusion of the PNS from the domain is particularly useful, as it avoids the severe Courant limitation imposed by resolving the PNS. The PNS is replaced by a rigid, spherical boundary, which contracts according to a prescription from a detailed spherically-symmetric-collapse calculation. This approach is designed to mimic the settling of material as the PNS cools.

By using all three of these simplifications, previous studies have been able to track the shock to large distances ($> 10^4$ km) and late times (> 1 s) (Scheck et al. 2004, 2006; Wongwathanarat et al. 2010). While useful for calculating long-term evolution, this approach requires inferring recoil through a rigid boundary of infinite inertial mass. Furthermore, this approach neglects effects resulting from the displacement of the PNS relative to the surrounding matter. To compensate for this effect, these authors have added a kick to the gas which mimics movement of the PNS. The physical fidelity of such approximations has been verified by self-consistent calculations such as those presented in (Nordhaus et al. 2010a) and in this work.

Recently, Nordhaus et al. (2010a) presented the first axisymmetric, multi-group, flux-limited diffusion neutrino transport calculation of recoil in which core collapse lead to significant acceleration of a fully-formed PNS. The authors used the multi-group, arbitrary Lagrangian-Eulerian (ALE), radiation-hydrodynamics code VULCAN/2D (Livne 1993). The calculation employed multi-group flux-limited diffusion neutrino transport (Livne et al. 2004), supplemented the neutrino luminosity by an additional $L_{\nu_e} = L_{\bar{\nu}_e} = 2 \times 10^{52} \text{ erg s}^{-1}$, and used the same $15 M_{\odot}$ progenitor as this work. During the induced, neutrino-driven explosion, a $\sim 10\%$ anisotropy in the ejecta led to a PNS recoil velocity of $\sim 150 \text{ km s}^{-1}$ at the end of the calculation, when the shock reached a radius of $\sim 5,000$ km. Such a result in terms of PNS velocity and ejecta asymmetry compares favorably with model $L_{2.2}$ presented in this work (see Table 1) and the results of Scheck et al. (2006).

In general, given the different computational techniques and the use of three different codes, the agreement between our results and those of Scheck et al. and Nordhaus et al. (2010a) is gratifying. Our detailed calculations of the first second of post-bounce evolution produce high-velocity recoils comparable with those in Scheck et al. (2004, 2006) and Nordhaus et al. (2010a) while following the evolution of the PNS itself. Taken together, these studies strongly suggest

that asymmetric core-collapse supernovae naturally lead to acceleration of the PNS and are capable of birthing the highest velocity pulsars.

While axisymmetry would restrict core motion to the Z -axis, 3D computations impose no such constraint and allow one to measure the PNS spin in addition to recoil. Recently, Wongwathanarat et al. (2010) presented the first 3D excised-core calculations of recoil. High PNS velocities were achieved for rotating and non-rotating progenitors, providing further evidence that PNSs are naturally accelerated during core collapse. However, in the case of pulsar spins, Rantsiou et al. (2011) showed that excising the PNS from the computational domain can lead to qualitatively different results in the spin rates. As such, future 3D calculations which include the PNS should be performed and differences between kicks from different progenitor models (rotating and non-rotating) should be investigated.

5 CONCLUSIONS

We have carried out a suite of axisymmetric simulations of the collapse of a massive star's core with the AMR, radiation-hydrodynamic code CASTRO. For each calculation, we follow the core collapse, PNS formation, ensuing neutrino-driven supernova explosion and PNS recoil. By incorporating the effects of neutrino heating and cooling in place of more detailed and computationally expensive neutrino transport, we are able to perform multiple calculations that simultaneously follow the evolution of the PNS and the global explosion for ~ 1 second and to distances of $\sim 10,000$ km.

The PNSs in our simulations achieved recoil velocities comparable to the those of observed pulsars. After ~ 1 second of post-bounce evolution, the highest PNS velocity obtained was 620 km s^{-1} (model L_{2.3}). After ~ 0.6 seconds of post-bounce evolution, this acceleration was supplied primarily by the gravitational pull of slow-moving ejecta in front of the PNS. This gravitational effect dominates the late-time PNS acceleration in all of our calculations. While our PNSs have started to decouple from the surrounding fluid (see Fig. 3), the substantial and ongoing gravitational acceleration suggests that higher velocities may ultimately be achievable.

Our results suggest that hydrodynamic recoil during an asymmetric supernova explosion provides a natural explanation for pulsar kicks. After the bounce shock stalls, hydrodynamic instabilities deform the shocked material and ensure that the ensuing explosion is asymmetric. Recoil during the supernova explosion and gravitational interaction with the expanding ejecta subsequently accelerate the PNS to high velocities. The results presented in this work are consistent with the findings of Nordhaus et al. (2010a) and previous axisymmetric simulations that excised the PNS from the computational domain (Scheck et al. 2004, 2006). Taken together, these studies strongly suggest that generic core-collapse supernovae can accelerate neutron stars to the high velocities observed in the pulsar population. Additionally, these studies demonstrate that hydrodynamic processes, and not asymmetric neutrino emission, are responsible for this acceleration (Scheck et al. 2006; Burrows et al. 2007b; Nordhaus et al. 2010a). In fact, recent simulations of neutron star

kicks in three dimensions suggest that velocities comparable to those from axisymmetric calculations are achievable (Wongwathanarat et al. 2010).

In this work, we have provided substantial numerical support to the hydrodynamic mechanism of pulsar kicks. Recoil due to a neutrino-driven, core-collapse supernova explosion provides a natural explanation for pulsar kicks without appealing to more exotic scenarios. As computational methods and resources improve, self-consistent three-dimensional studies will enable a full comparison of theoretical models to observed distributions of pulsar kicks and spins.

ACKNOWLEDGEMENTS

The authors thank Noam Soker, Thomas Janka, Annop Wongwathanarat and Ewald Mueller for comments which lead to an improved manuscript. JN is supported by an NSF Astronomy and Astrophysics Postdoctoral Fellowship under award AST-1102738 and by NASA HST grant AR-12146.04-A. TBD is supported by an NSF Graduate Research Fellowship under grant number DGE-0646086. AB is supported by the Scientific Discovery through Advanced Computing (SciDAC) program of the DOE, under grant DE-FG02-08ER41544, the NSF under the subaward ND201387 to the Joint Institute for Nuclear Astrophysics (JINA, NSF PHY-0822648), and the NSF PetaApps program, under award OCI-0905046 via a subaward 44592 from Louisiana State University to Princeton University. Work at LBNL was supported in part by the SciDAC program under contract DE-FC02-06ER41438. AA is supported by the Office of High Energy Physics and the Office of Mathematics, Information, and Computational Sciences as part of the SciDAC Program under the U.S. Department of Energy under contract No. DE-AC02-05CH11231. The authors thank the members of the Center for Computational Sciences and Engineering (CCSE) at LBNL for their invaluable support for CASTRO.

Support for HPC storage and resources was provided by the National Energy Research Scientific Computing Center (NERSC), which is supported by the Office of Science of the US Department of Energy under contract DE-AC03-76SF00098; by NICS, on the Kraken supercomputer, provided by the National Science Foundation through the TeraGrid Advanced Support Program under grant TG-AST100001; by the TIGRESS High Performance Computing and Visualization Center at Princeton University, which is jointly supported by the Princeton Institute for Computational Science and Engineering (PICSciE) and the Princeton University Office of Information Technology.

REFERENCES

- Almgren, A. S., Beckner, V. E., Bell, J. B., Day, M. S., Howell, L. H., Joggerst, C. C., Lijewski, M. J., Nonaka, A., Singer, M., and Zingale, M.: 2010, *ApJ* **715**, 1221
- Barkovich, M., D'Olivio, J. C., and Montemayor, R.: 2004, *Phys. Rev. D* **70**(4), 043005
- Bethe, H. A. and Wilson, J. R.: 1985, *ApJ* **295**, 14
- Blondin, J. M. and Mezzacappa, A.: 2007, *Nature* **445**, 58
- Blondin, J. M., Mezzacappa, A., and DeMarino, C.: 2003, *ApJ* **584**, 971

- Brandt, T. D., Burrows, A., Ott, C. D., and Livne, E.: 2011, *ApJ* **728**, 8
- Buras, R., Rampp, M., Janka, H., and Kifonidis, K.: 2006, *A&A* **447**, 1049
- Burrows, A., Dessart, L., Ott, C. D., and Livne, E.: 2007a, *Phys. Rep.* **442**, 23
- Burrows, A. and Hayes, J.: 1996, *Physical Review Letters* **76**, 352
- Burrows, A., Hayes, J., and Fryxell, B. A.: 1995, *ApJ* **450**, 830
- Burrows, A., Livne, E., Dessart, L., Ott, C. D., and Murphy, J.: 2007b, *ApJ* **655**, 416
- Cen, R.: 1998, *ApJ* **507**, L131
- Chatterjee, S., Vlemmings, W. H. T., Briskin, W. F., Lazio, T. J. W., Cordes, J. M., Goss, W. M., Thorsett, S. E., Fomalont, E. B., Lyne, A. G., and Kramer, M.: 2005, *ApJ* **630**, L61
- Faucher-Giguère, C. and Kaspi, V. M.: 2006, *ApJ* **643**, 332
- Fernández, R.: 2010, *ArXiv e-prints*
- Fernández, R. and Thompson, C.: 2009, *ApJ* **703**, 1464
- Fujimoto, S.-i., Kotake, K., Hashimoto, M.-a., Ono, M., and Ohnishi, N.: 2011, *ApJ* **738**, 61
- Fuller, G. M., Kusenko, A., Mocioiu, I., and Pascoli, S.: 2003, *Phys. Rev. D* **68(10)**, 103002
- Gunn, J. E. and Ostriker, J. P.: 1970, *ApJ* **160**, 979
- Hanke, F., Marek, A., Mueller, B., and Janka, H.-T.: 2011, *ArXiv e-prints*
- Hansen, B. M. S. and Phinney, E. S.: 1997, *MNRAS* **291**, 569
- Hobbs, G., Lorimer, D. R., Lyne, A. G., and Kramer, M.: 2005, *MNRAS* **360**, 974
- Hwang, U. and Laming, J. M.: 2011, *ArXiv e-prints*
- Janka, H.: 2001, *A&A* **368**, 527
- Khokhlov, A. M., Höflich, P. A., Oran, E. S., Wheeler, J. C., Wang, L., and Chtchelkanova, A. Y.: 1999, *ApJ* **524**, L107
- Kishimoto, C. T.: 2011, *ArXiv e-prints*
- Kusenko, A. and Segrè, G.: 1999, *Phys. Rev. D* **59(6)**, 061302
- Lai, D., Chernoff, D. F., and Cordes, J. M.: 2001, *ApJ* **549**, 1111
- Lai, D. and Qian, Y.: 1998, *ApJ* **505**, 844
- Lambiasi, G.: 2005, *Phys. Rev. D* **71(6)**, 065005
- Liebendörfer, M., Rampp, M., Janka, H., and Mezzacappa, A.: 2005, *ApJ* **620**, 840
- Livne, E.: 1993, *ApJ* **412**, 634
- Livne, E., Burrows, A., Walder, R., Lichtenstadt, I., and Thompson, T. A.: 2004, *ApJ* **609**, 277
- Lyne, A. G. and Lorimer, D. R.: 1994, *Nature* **369**, 127
- Marek, A. and Janka, H.: 2009, *ApJ* **694**, 664
- Murphy, J. W. and Burrows, A.: 2008, *ApJ* **688**, 1159
- Nardi, E. and Zuluaga, J. I.: 2001, *ApJ* **549**, 1076
- Nordhaus, J., Brandt, T. D., Burrows, A., Livne, E., and Ott, C. D.: 2010a, *Phys. Rev. D* **82(10)**, 103016
- Nordhaus, J., Burrows, A., Almgren, A., and Bell, J.: 2010b, *ApJ* **720**, 694
- Ott, C. D., Burrows, A., Dessart, L., and Livne, E.: 2008, *ApJ* **685**, 1069
- Papish, O. and Soker, N.: 2011, *MNRAS* **416**, 1697
- Rantsiou, E., Burrows, A., Nordhaus, J., and Almgren, A.: 2011, *ApJ* **732**, 57
- Sawai, H., Kotake, K., and Yamada, S.: 2008, *ApJ* **672**, 465
- Scheck, L., Kifonidis, K., Janka, H., and Müller, E.: 2006, *A&A* **457**, 963
- Scheck, L., Plewa, T., Janka, H., Kifonidis, K., and Müller, E.: 2004, *Physical Review Letters* **92(1)**, 011103
- Shen, H., Toki, H., Oyamatsu, K., and Sumiyoshi, K.: 1998, *Nuclear Physics A* **637**, 435
- Wongwathanarat, A., Janka, H.-T., and Müller, E.: 2010, *ApJ* **725**, L106
- Woosley, S. E. and Weaver, T. A.: 1995, *Astrophys. J. Supplements* **101**, 181
- Zhang, W., Howell, L., Almgren, A., Burrows, A., and Bell, J.: 2011, *ApJS* **196**, 20
- Zou, W. Z., Hobbs, G., Wang, N., Manchester, R. N., Wu, X. J., and Wang, H. X.: 2005, *MNRAS* **362**, 1189